Journal of Alloys and Compounds 822 (2020) 153555

Contents lists available at ScienceDirect

Journal of Alloys and Compounds

journal homepage: http://www.elsevier.com/locate/jalcom

First-principles study of the insertion and diffusion of interstitial atoms (H, C, N and O) in nickel

Matthieu David , Aurélien Prillieux , Daniel Monceau , Damien Connétable *

CIRIMAT, UMR 5085, CNRS INP UPS, ENSIACET, 4, Allée Émile Monso, BP 44362, F-31030, Toulouse Cedex 4, France

ARTICLE INFO

Article history:
Received 2 June 2019
Received in revised form
24 December 2019
Accepted 26 December 2019
Available online 7 January 2020

Keywords:
nickel
Interstitial species
DFT
Diffusion
Solubility

ABSTRACT

Solubility and diffusivity of interstitials in Ni is of prime importance to understand and quantify reactivity of Ni-base structural alloys at high temperature. We thus present a first-principles study of the insertion and diffusivity of interstitial species in nickel. We put an emphasis on carbon, nitrogen and oxygen atoms and compare our results with those found for hydrogen and in the literature. The interactions with the metal and the relative stability of sites are discussed in detail in terms of phonon, electronic, elastic, magnetic properties and charge transfers. As a result, we identified one new stable interstitial position for C and N atoms, and we also showed that the tetrahedral site can be considered as unstable from an elastic standpoint for carbon. In the light of these new results, diffusion mechanisms were reviewed and diffusion coefficients were calculated. The effects of temperature on enthalpy and migration energies were investigated. We thus showed that C and N atoms on one hand, H and O atoms on the other hand, show the same behavior.

1. Introduction

Interstitial elements in Ni based alloys play a major role in many physical phenomena such as environmental embrittlement, cementation, precipitation, phase transitions or changes in physical properties. Hydrogen is known to be at the origin of the embrittlement of many metals [1]. C atoms can lead to carburation and to metal dusting [2], it can be involved in the formation of carbides with many species [3], thereby inducing mechanical reinforcements of nickel alloys, and segregate at grain boundaries and interfaces. Oxygen forms oxides and cause internal and intergranular oxidation [4,5] which may lead to stress corrosion cracking [4]. N atoms are a solid solution strengthening element for steels [6] and form Ti and Al nitrides in nickel based super-alloys [7]. Understanding the behavior of interstitial atoms in metallic systems is a key step in the knowledge of micro-structural evolution. The amount and kinetics of elements insertion and of induced precipitation is controlled by C, H, N, and O permeability [5]. It is thus crucial to accurately determine the solubility and diffusivity of species responsible for the physical phenomena that are being studied.

For interstitial species, the lattice composed of atoms, here Ni, can be seen as imposing a fixed energy landscape in which these atoms are inserted and diffuse more or less freely. However, contrary to what was done in earlier works [8,9], a stronger focus should be put on the stability of interstitial sites by studying the full inter-atomic constants when interstitial sites are filled, as it was recently done in the case of aluminum [10]. Stable configurations strongly depend on interactions between the metal and interstitial species, leading to different stable positions, as found in earlier literature. This information is a prerequisite for studying diffusion mechanisms at the atomic scale. Indeed, in the case of interstitial elements, the elementary mechanisms, which are supposed to be limited, reveal a complex landscape depending on the specie [10,11], especially when atoms interact strongly with the metal.

The aim of this work is thus twofold. First, we show that interstitial atoms in fcc systems are not necessarily located in usual interstitial sites and that special attention should be paid to phonon properties. We also discuss the use of elastic modeling for interstitial species. Secondly, we show that the diffusion coefficient formulas classically used do not always apply. Hereinafter, the study is limited to “interstitial” positions, the formation of clusters [12,13] is not considered in the present work.

The first step consists in the investigation of stable configurations using first-principles approaches. An accurate analysis of stable sites was conducted including a new stable position called *M*.

* Corresponding author.
E-mail address: damien.connetable@ensiacet.fr (D. Connétable).

https://doi.org/10.1016/j.jallcom.2019.153555
0925-8388/

Previous works (on carbon [8,9], oxygen [9,14] or hydrogen [15]) have shown that octahedral (*o*) sites are the most stable positions, that tetrahedral sites (*t*) are the second most stable, and that mechanisms of diffusion involve *o*-*t* and *o*-*o* paths. We thus take this opportunity to present an overview of the insertion of single species and of the interactions between the metal and interstitial species. We try to show how interstitial species interact with nickel at the atomic scale, but also at a larger scale by computing elastic dipoles and electronic properties.

Based on these results and structure analyses, we studied the escape rate of different paths, i.e. trajectories, barriers energies and frequencies attempts were investigated. In earlier literature [8,9,15] simple mechanisms were considered, without discussing in detail the stability of sites. We thus attempt to revisit the diffusion coefficients of C, O and N atoms in nickel considering the *M* position (see Ref. [10]) and including phonon energy by means of full vibrations of the systems. The effect of temperature on diffusion coefficients were also evaluated within the quasi-harmonic approximation, at several temperatures based on lattice expansion calculations, as explored by Wimmer [15] for H atoms in nickel.

For this purpose, the article is organized as follows. The first part (section 2) summarizes the simulation method. In section 3, insertion in Ni was investigated: stability of the interstitial, with a particular emphasis on interactions between the metal and interstitial on the different sites. Finally, in section 4, we present a study of the diffusion mechanisms at the atomic scale. The diffusion coefficients based on explicit formulas is therefore presented and compared to experimental findings. The effects of temperature are presented and results are compared to those found in the literature.

2. Computational details

First-principles calculations were performed with the density functional theory (DFT) using the VASP code (Vienna *ab initio* simulation package) [16]. The Perdew-Burke-Ernzerhof [17] generalized gradient approximation of the exchange and correlation functional was used for all calculations, and the PAW method [18,19] was adopted. The magnetism was taken into account in all calculations (for bulk and references states as well) using collinear spin polarized calculations. Calculations give a magnetic moment for nickel equal to 0.62 μ_B per atom, in excellent agreement with the experimental data [20].

Calculations were performed at zero pressure, lattice parameters and shapes of super-cells were fully relaxed. Atomic forces were always lower than 0.01 eV/Å on atoms. The plane-wave cut-off energy was set to 600 eV. The study of the insertion (in the dilute solution) were carried out on two super-cells ($2 \times 2 \times 2$ and $3 \times 3 \times 3$ super-cells, i.e. 32 and 108 atoms per unit-cell, respectively) with full periodic boundary conditions. The first-Brillouin zones were sampled by $10 \times 10 \times 10$ and $6 \times 6 \times 6$ Monkhorst-Pack **k**-mesh grids [21]. The precision reached was about 2–3 meV/atom. The insertion energies of the largest super-cells were considered sufficiently accurate to correspond to the energy of isolated species (dilute limit).

The frequencies and inter-atomic force constants (IFC) were computed using the finite displacements method on $2 \times 2 \times 2$ super-cells, to limit numerical costs, for the interstitial positions and transitions states. The *phonopy* package [22] was used to generate finite displacements according to the symmetry of each structure. It was then used to analyze, to plot phonon properties (phonon dispersion curves and density-of-states, not always shown here) and to compute Helmholtz free energies. A cut-off energy of 600 eV, an electronic convergence criteria of 10^{-6} eV and fine **k**-mesh grids ($10 \times 10 \times 10$) were used.

Migration paths were investigated on $2 \times 2 \times 2$ and $3 \times 3 \times 3$ super-cells. We used the climbing-image nudged elastic band method (CI-NEB) with the formulation suggested by Henkelman group [23], using an optimizer [24] for more efficiency while searching for the minimum energy path (MEP). The main advantage of the CI-NEB method is that it is possible to calculate the transition state (TS) and optimize the volume shapes at the same time. Reaction paths were sampled with five intermediate images. MEP identification was performed through two steps: *(i)* first, pre-convergence was achieved using a less precise parameter set ($3 \times 3 \times 3$ **k**-mesh grids and a cut-off energy of 400 eV); and *(ii)* energies were then performed with the same convergence parameters as for the study of point defects (cut-off energy of 600 eV and $10 \times 10 \times 10$ **k**-mesh grids, for $2 \times 2 \times 2$ super-cells).

Finally, thermal effects were partially incorporated, taking into account the thermal expansion of the lattice within the framework of the quasi-harmonic approximation. We assessed thermal effects on migration and solubility energies. The lattice expansion method was used to include thermal effects. We assumed in this work that interstitial elements do not induce specific lattice distortions with temperature: we therefore used the lattice thermal expansion of the perfect nickel fcc structure. The lattice parameters were calculated using the expression proposed by Wimmer et al. [15]:

$$a(X_i,T) = a_o(X_i) + 2.774 \times 10^{-5}T + 2.282 \times 10^{-8}T^2 - 5.243 \times 10^{-12}T^3 + 3.629 \times 10^{-16}T^4 \quad (1)$$

where $a_o(X_i)$ (in Å) is the lattice constant of one super-cell containing a fraction of X atom (X = C, N or O) occupying the *i* site (*o*, *t* or *M*). $3 \times 3 \times 3$ super-cells (108 Ni atoms + 1 X atom) were used to compute formation energies, whereas Helmholtz free energies were computed on $2 \times 2 \times 2$ super-cells. The lattice parameters of the intermediate super-cells constituting the NEB were thus interpolated between initial and final configurations as is usually done with this method. Calculations were thus conducted at 600, 1200, 1500 and 1800K.

3. Solubility

3.1. Stability at 0 K

The insertion energy, $E^s[X_i]$, is used to quantify the insertion of an atom *X* in nickel in the site *i*:

$$E^s[X_i] = E_o[n.Ni + X_i] - E_o[n.Ni] - E_{ref}[X] \quad (2)$$

$E_o[n.Ni+X]$ and $E_o[n.Ni]$ are the DFT values of super-cells (composed of *n* Ni atoms) with and without an interstitial element, respectively. $E_{ref}[X]$ corresponds to the energy (per X atom) of the reference state of the X atom (molecule or diamond, see Appendix A). A positive (resp. negative) $E^s[X_i]$ value corresponds to the energy gained (resp. lost) when the *X* atom occupies an *i* site. We considered octahedral (in *4b* position in the fcc system, space group 225) and tetrahedral (*8c*) sites. Results of simulations are listed in Table 1.

Details below show that results obtained using the PBE functional at 0 K are comparable, quantitatively and qualitatively, with previous works [8,13,15,25–27].

First, as found in earlier works [9,15], all interstitial species prefer to occupy the octahedral positions (*o* sites) of the nickel fcc-lattice. The energy difference, ΔH (including the zero-point energy, see section 3.2), between *o* and *t* sites is equal to 0.34, 1.54, 1.05 and 0.20 eV for H, C, N and O, respectively. Results are in good agreement with earlier theoretical works: about 0.25 eV in the case of H [13,15,25,26], 1.53 eV for carbon [8,9] and 0.17 eV for O atoms [27].

Table 1
Insertion ($E^s[X]$, in eV) and zero-point energies ($F_{0K}[X]$, in eV), solubility enthalpies ($H^s = F_{0K}[X] + E^s$, in eV). ΔH is the energy difference between *i* and *o* sites.

X		E^s	$F_{0K}[X]$	H^s	ΔH
H	*o*	0.063	0.005	0.068	0
	t	0.323	0.084	0.407	0.34
	M	0.814	unstable		
C	*o*	0.586	0.089	0.675	0
	t	2.277	−0.057	2.220	1.54
	M	2.167	0.035	2.201	1.53
N	*o*	0.702	0.011	0.713	0
	t	1.762	0.003	1.765	1.05
	M	2.239	−0.032	2.207	1.49
O	*o*	0.468	−0.019	0.449	0
	t	0.646	0.004	0.650	0.20
	M	1.265	unstable		

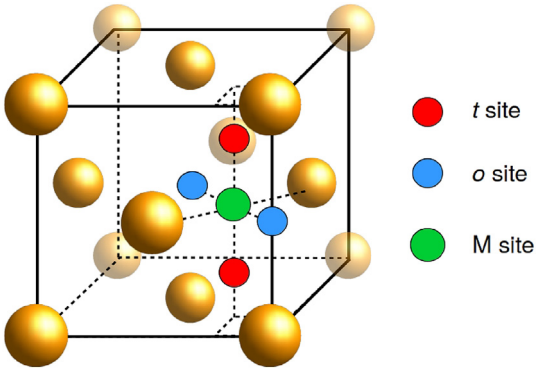

Fig. 1. Schematic representation of interstitial *t*, *o* and *M* sites.

From these energies, it is possible to distinguish two groups: on one side, H and O atoms, where ΔH is low (<0.5 eV), and on the other side, C and N atoms, where ΔH is high, >1 eV. This classification will be confirmed considering the following results.

It had been shown in a recent work on aluminum [10] that there is another possible stable position in fcc systems: the *M* site (with the Wyckoff position *24d*), see Fig. 1. This configuration, located exactly at the midpoint of two first-nearest-neighboring Ni atoms, is also located at the midpoint of two *o* and two *t* sites. It had been identified as being a (second-order) transition state in the *o*-*o* path for hydrogen in many fcc-metals [28], although, as seen in Al, *M* is a stable position for C and B atoms.

We therefore investigated this additional site and calculated its insertion energy for all species. DFT values are given in Table 1. Results show that this site is always stable from a geometrical standpoint. The *M* site is more stable than the *t* site for C atoms, almost 100 meV lower in energy, while in the case of H, O and N atoms, it is found less stable than *t* sites (about 0.5 eV). At this level, it is not possible to rule on their stability, i.e it is not possible to know if it is local minimum or maximum. Substitution was also considered, but in all cases, it was found unstable. The atoms move from the ideal position and prefer to form clusters as shown in the case of H [13,25,29] or of O atoms [27]. *In fine*, these new results do not change the physics of H, C, N and O insertion in the nickel, since the most stable positions are always the *o* sites.

DFT values can now be compared against experimental ones. Experimentally, the solubility energy is deduced by fitting the content of species measured with an Arrhenius law or a Sieverts law for dilute solutions. The Sieverts law [30] relies the amount of species (here hydrogen, $C[Hy]$) dissolved in the system and the temperature:

$$C[Hy] \propto \sqrt{\frac{p_{H_2}}{p_o}} \exp\left[-\frac{H^s}{k_B T}\right], \tag{3}$$

where p_o is equal to 1 atm, p_{H_2} the pressure of the gas, and H^s the solubility energy. It corresponds to the situation where there is a thermal equilibrium between a solid solution (H in insertion) and H_2 gas: $Ni + 1/2xH_2 \rightleftharpoons NiH_x$ ($x \ll 1$). DFT values of H^s can thus be directly compared with experimental values. Taking into account the experimental and simulation uncertainties, the result for hydrogen in the *o* site (+0.07 eV) is in agreement with experimental data (+0.17 eV) [31]. This reflects an equilibrium without hydrides or clusters formed in the metal. It should be noticed that the content of VH_n clusters is always negligible in Ni, for common experimental conditions, see Ref. [32].

About the O atom, Connétable et al. [27] have already shown that there is a strong disagreement between theoretical and experimental values: at 0 K, calculations give 0.46 eV, whereas experimental measurements range between [-2.5; −1.8] eV depending to the experimental conditions [33–35]. This discrepancy is in part due to the reference state (here the O_2 molecule) which is badly described in DFT due to an overestimation in the GGA of the O_2 molecule binding. Wang et al. [36] have therefore applied an energy shift of 1.4 eV per O_2 molecule to reproduce experimental value of the formation energy of oxides. This value, associated with temperature effects on the chemical potential, could partially reconcile experimental and theoretical values. However, there are other arguments to explain this disagreement. The formation of VO_m clusters could also explain this difference. As shown in Ref. [27], O atoms strongly interact with nickel to form clusters. A thermodynamic analysis showed that, even at high temperature, O atoms are mainly located in these clusters and are not isolated in nickel. The DFT value was computed in the dilute limit. The Sieverts law is also used in the case of O atoms to determine H^s [34]. However, measurements were often made under experimental conditions such that the pressure p_{O_2} is sufficient to form NiO oxide layers on the surface [33,34]. The chemical potential of the O atom is thus not the gas but the oxide, and the Sieverts' law should be thus not valid. These arguments let us think that the link between theory and experimental observations is hard to reconciliate.

In the case of C atoms, there are few reported values of solubility in pure nickel. The solubility of C has been determined by Dunn et al. [37] and values reported are in the magnitude order of 10^{-2} atomic fraction near the melting point. Insertion energies reported are thus in the range of 0.42–0.49 eV (high-temperature measurements of the carbon solubility). These are in good agreement with our results obtained at 0 K.

Finally, in the case of nitrogen, there are no experimental data in the nickel crystal. Values found in literature only refer to the solubility of nitrogen in liquid pure nickel and nickel based alloys [38–41]. In these cases, experimental observations show a low solubility of N in nickel (as for carbon). This must translate into high solubility energy, which is consistent with our result, where the insertion energy in *o* sites is 0.7 eV.

3.2. Vibrational properties

We now discuss the stability of the sites by computing interatomic force constants. Phonon band structures (*pBAND*) are displayed in Fig. 2. Substituted sites were also studied, but, for simplicity, not represented here.

When phonon branches are all positive, the configuration can be considered as stable, otherwise the configuration is unstable. When imaginary frequencies are associated with the interstitial element,

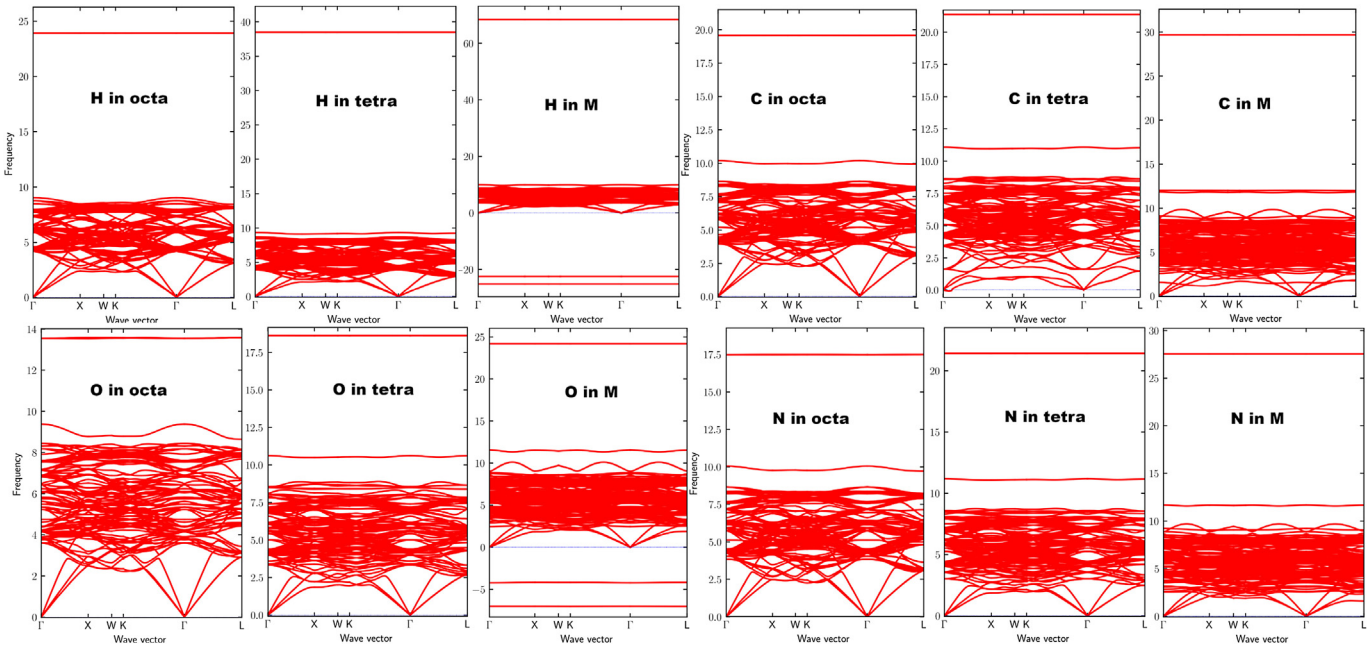

Fig. 2. Phonon band structures for a system with one atom (H, C, N and O atoms) in an interstitial position, either in *o*, *t* or *M* sites. Negative bands correspond to imaginary frequencies. Energies (frequencies) are expressed in THz.

with a degeneracy of one, the configuration should probably be near a first-order transition state (for the X atom), and when the degeneracy is double or triple, the configuration does not meet the conditions for being a first-order transition state and is unstable.

In the case of H and O atoms, *t* and *o* sites are stable, whereas *M* sites present two imaginary vibrations, associated with the interstitial elements. It is thus a second-order transition state, see the discussion in Ref. [28]. Such configuration plays a negligible effect on the diffusivity, they will be neglected in the following.

In the case of carbon, while *M* and *o* sites are stable, we observe an anomaly for *t* sites. Indeed, when the *t* site is filled with carbon, *pBAND* exhibits a small acoustic instability in the Γ - *X* direction, see Fig. 2. In order to confirm this result, we conducted additional tests on 3 × 3 × 3 super-cells, as well as convergence tests. Again, we found this acoustic instability every time. These results suggest that, at least at low temperature, when a carbon occupies a *t* site, the structure becomes unstable. From a mechanical standpoint, acoustic branches are directly linked to the speed of sound velocity in crystals. They can thus be used to compute elastic constants, C_{ij}, see for instance Ref. [42]. In cubic systems, C_{11} and C_{44} must be positive. We thus computed them directly with another approach (using small strains on 3 × 3 × 3 super-cells) and found that C_{44} is negative. One of the three Born stability criteria (for cubic systems) is therefore not verified, see Mouhat [43]. Additional simulations were conducted to find other stable position(s) around the *t* sites, without success. When the C atom is pushed a little out the *t* site, towards either the *M* site or the *o* site, it always falls back in these positions. The *t* site is thus not a local minimum for carbon. This result is not in contradiction with the results on diffusion mechanisms found in the literature [8,9], where the transition state for the *o*-*t* path was always found to be located very close to the *t* site. It is not excluded that the effect of temperature could stabilize the *t* configuration, as it has been shown by Mei [44] in cubic vanadium nitride. However, temperatures should not change the fact that this site is less stable than *o* sites, and that the *t* site should be located in the vicinity of a transition state.

In the case of the N atom, the results show that all sites are stable, *M* sites as well.

At this stage, for H and O atoms, *o* and *t* sites are the stable positions, for N atoms, there are three configurations, and for C atoms, only *M* and *o* sites are stable positions.

From phonon frequencies, zero-point energies ($F_{0K}[X]$) were computed using molecules as reference states for H, N and O atoms, nd diamond for carbon (see Appendix A) as follows:

$$F^{0K}[X] = F^{0K}_{vib}[n.Ni + X] - F^{0K}_{vib}[n.Ni] - F^{0K}_{vib}\left[X_{ref}\right] \tag{4}$$

F_{vib} are the phonon Helmholtz free energy computed using IFC on fine **q**-mesh grids, here calculated at 0 K (labeled 0*K*).

$$F_{vib}(T) = k_B T \sum_{\nu=1}^{3N} \int n_\nu(\mathbf{q}) \ln\left[2\sinh\left(\frac{\hbar\omega_{\nu,\mathbf{q}}}{2k_B T}\right)\right] d\mathbf{q} \tag{5}$$

$\omega_{\nu,\mathbf{q}}$ are the frequencies in **q** and ν of the system. $F_{0K}[X]$ values are given in Table 1. Except H atoms, the $F_{0K}[X]$ is low compared to the solubility energy. This does not change the relative stability of sites.

Using phonon excitations, we also calculated the mean square displacements ($\overline{d_T}$) of X atoms in each site as a function of temperature [45], along the [010] direction for *o* and *t* sites and along the [010] and [101] directions for *M* sites. This quantity is used to evaluate the displacement/oscillations of X as a function of temperature:

$$\overline{d_T} = \langle \left| u^\alpha(jl,t) \right|^2 \rangle = \frac{\hbar}{2Nm_j} \sum_{\mathbf{q},\nu} \frac{(1 + 2n_\nu(\mathbf{q},T)) \left| \varepsilon^\alpha_\nu(j,\mathbf{q}) \right|^2}{\omega_{\nu,\mathbf{q}}} \tag{6}$$

j is the index of the j^{th} atom in the super-cell *l*, α corresponds to a crystallographic direction (here [010] or [101]). *m* and *N* are the atomic mass and the number of super-cells. **q** is the wave-vector, ν is the index of the phonon mode. $\varepsilon_\nu(j,\mathbf{q})$ is the associated polarization vector. $\nu(\mathbf{q},T)$ is the Boson distribution:

Table 2
Atomic Bader charge, $\mathscr{B}$, are in electron unit. In parentheses, we give the electron number of the X atom. $\overline{d}_T[X]$ (in Å) is the mean square displacement of the X atom computed at 0 and 1200 K, along the [010] direction for *o* and *t* sites, and along the [010] and [101] directions for *M* sites.

X		$\overline{d_0}[X]$	$\overline{d}_{1200}[X]$	$\mathscr{B}$
H	*o*	0.15	0.26	1.3 (1)
	t	0.12	0.21	1.3 (1)
C	*o*	0.05	0.14	4.9 (4)
	t	–	–	4.6 (4)
	M	0.06/0.12	0.18/0.12	4.8 (4)
N	*o*	0.05	0.13	6.0 (5)
	t	0.06	0.19	5.8 (5)
	M	0.08/0.09	0.30/0.12	6.0 (5)
O	*o*	0.06	0.16	7.1 (6)
	t	0.05	0.17	6.9 (6)

Table 3
Elastic constants (in GPa) deduced from acoustic branches (calculated on $2 \times 2 \times 2$ super-cells): C_{11}, C_{44}, C_{12} and $C' = (C_{11} - C_{12})/2$. We used the same approach as the one presented in Ref [42]. Results for the bulk are compared to the experimental [46] and theoretical literature [47]. The accuracy on the fit is equal to about ± 3 GPa. For the bulk, the value of C_{11} is in excellent agreement with literature. We strongly underestimate C_{44} and C_{12} values.

X	C_{11}	C_{44}	C_{12}	C'
bulk (sound velocity)	274	116	106	75
GGA [47]	274	130	160	57
Exp [46].	261	131	150	55
H	269	117	108	73
C	267	118	100	70
N	266	118	100	70
O	261	111	89	69

$$n_\nu(\mathbf{q}, T) = [\exp(\hbar\omega_\nu(\mathbf{q})/k_B T) - 1]^{-1} \quad (7)$$

Data at 0 and 1200 K are listed in Table 2.

$\overline{d}_T$ are found smaller in *o* sites than in *t* sites; frequencies of X atoms in *t* sites are indeed always higher in energy than those in *o* sites. The volumes induced by phonon excitations in *o* and *t* sites are thus small (< 0.1 Å^3), even at high temperature, smaller than the volume of formation for instance (see below). The most interesting cases are for *M* sites. Vibrations of N and C atoms at 1200 K in *M* induce a large displacement, approximately 0.2–0.3 Å, along the directions perpendicular to the Ni–Ni bonds (i.e., [010] for example). As stated hereinafter, atoms thus move/vibrate beyond the position of the transition state in the *o*-*o* or *t*-*t* paths. C and N atoms will not stay in *M* sites at high T. They could be considered as unstable at high T.

We finally evaluated, from the slopes of the acoustic branches around the $\mathbf{q} = \Gamma$ point, elastic constants [46]. Three directions were used to compute them: [100], [111] and [110]. Results are given in Table 3 for a high concentration in interstitial specie (here 3% atomic, i.e. one X atom for 32 Ni atoms). From these results, we can have a qualitative idea of the effect of insertion on the elastic properties of nickel.

Oxygen, and in to a lesser extent, C and N atoms, lead to a decrease in elastic properties. However, we can see that the effect of H atoms is negligible (in the numerical error).

3.3. Charge transfers

The effect of insertion on the electronic and magnetic properties of the metal, as well as charge transfers are now going to be investigated. The Bader charge [48] is the first parameter that was examined. Values are listed in Table 2. Except for the H atom, whose the Bader charge transfer ($\mathscr{B} - e$, where $\mathscr{B}$ and e are respectively the Bader charge and the atomic charge) is lower and equal to about $+0.3e$, atoms located in *o* sites attract part of the charge of 1NN Ni atoms. The charge transfer for C, N and O atoms is thus equal to about +0.9, +1.0 and + 1.1 *e*. The charge decrease of 1NN Ni atoms (not given here) is slightly if carbon atoms are located in *o* sites rather than in *t* or *M* sites, for which the charge transfer is similar. In the case of O atoms occupying *o* or *t* sites, this charge decrease was found smaller, and for N atoms occupying *o* and *t* sites, it was found identical.

To illustrate this charge transfer, Fig. 3 displays contour maps associated with charge transfers $\Delta\rho$, when *o*, *t* and *M* sites are filled with an impurity, i.e.:

$$\Delta\rho = \rho[bulk + X] - \rho[bulk] - \rho[X] \quad (8)$$

where $\rho[Y]$ are the DFT charge densities of the *Y* system. The case of H atom is also depicted for comparison purposes.

By comparing the charge density difference between the species for a given site (*o* or *t*), it can be noticed that the shapes of $\Delta\rho$ are similar. The main difference lies in the range of this charge transfer: stronger and more localized for O atoms than for N and C atoms, in agreement with the Bader charge analysis presented above. Nevertheless, the charge transfer is different for H atoms: it is not only significantly smaller than that of other species, but also highly isotropic and at low scale. The shape is close to a sphere for both *o* and *t* sites, which is comparable to the shape of the *s* orbitals of the hydrogen atom. For *M* sites, the charge accumulation is slightly higher for C atoms than for N atoms and has the shape of *p* orbitals. As expected, in *M* sites, atoms form strong bonds with 1NN Ni atoms. C, N and O atoms thus form bonds with the 1NN Ni atoms. These elements improve the mechanical properties of nickel, as shown above.

Finally, a slightly negative charge ring (blue zone) can be observed around the interstitial site. The charge ring of *o* site increases with the number of valence electrons from C to O. This is due to the covalent bond between X atoms and the metal, especially in the case of oxygen.

3.4. Projected electronic densities-of-states

The electronic density-of-states (*eDOS*) provides complementary information regarding the relative stability of sites and allows to highlight the nature of the bonds between atoms. The *eDOS* of the interstitial species projected on *s*, *p* and *d* orbitals are displayed in Figs. 4 and 5. Spin up and down contributions were both drawn.

In the case of H atoms, Fig. 4, it can be noted that, (i) there is little change in the *eDOS* around the Fermi level, $\varepsilon_{\mathscr{F}}$, (ii) the hybridization between the H and Ni states is located $[-9; -8]$ eV below $\varepsilon_{\mathscr{F}}$. New peaks of the *d*, *p* and *s* Ni states appear where the hydrogen *s* states are present. This result fits well with charge transfers, Fig. 3. In the case of *t* sites, we note that the *d* states of 1NN Ni atoms are highly modified around $\varepsilon_{\mathscr{F}}$ (small peak), explaining (Hume-Rothery rule) why the configuration is energetically less stable than the *o* site. For oxygen, the hybridization between 1NN Ni and O atoms modifies the magnetism of one electronic spin only. The *p* states of O atoms interact with all states of Ni atoms, showing a strong interaction with the metal.

For carbon and nitrogen in *t*, *o* and *M* sites, whose *eDOS* are displayed in Figs. 4 and 5. Their *s* states (not shown to lighten the graphs) are located at lower energy, around −12.8 and −17.3eV below $\varepsilon_{\mathscr{F}}$ for C and N atoms, respectively. These species interact

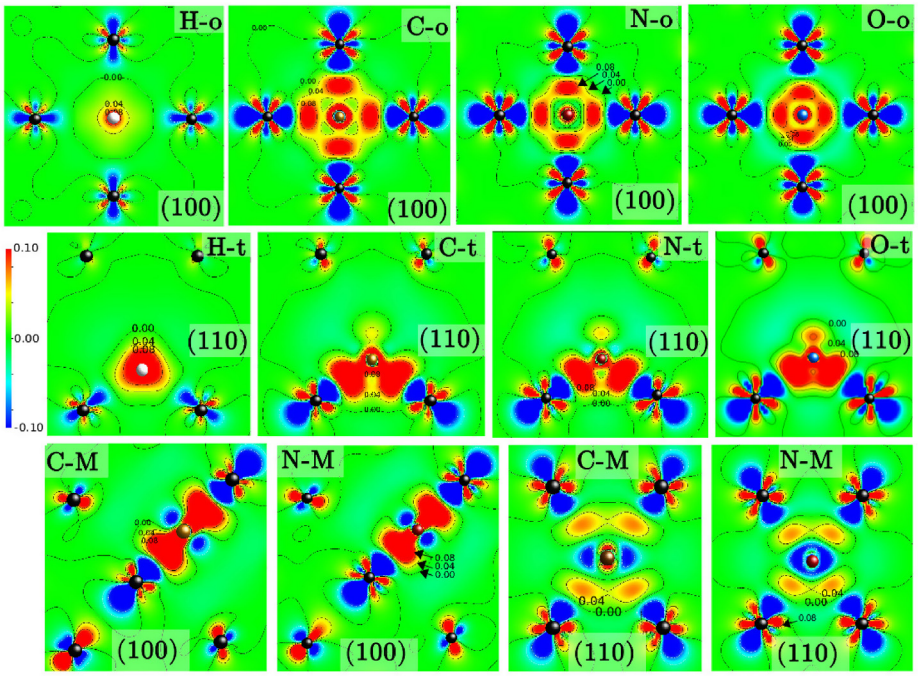

Fig. 3. Plot of contour maps of the charge transfer, $\Delta\rho$ (in e/Å^3), when sites are filled: for H, C, N and O atoms in their different stable configurations. The same scale was used for all plots.

mainly with the metal through their *p* shells. Part of the *s*-states density of the carbon lies on a broad energy value (between −8.25 and -3eV) that overlays the *s*- and *d*-states of 1NN Ni atoms. Peaks in the *p*-shells of C and N atoms range from $[-7; -5.5]$ eV. These are in interaction with Ni states, essentially with the *d* shells of 1NN Ni atoms. This can explain the charge transfer between the *p* and *d*, and *s* states.

3.5. Magnetic moment

As seen above, when an atom occupies either a *t*, a *o* or a *M* site, a small part of the electrons of first- (and, to a lesser extent, second-) nearest neighbors Ni atoms of the interstitial are transferred towards the interstitial. We can also presume that this leads to a (small) modification of the local atomic magnetic moment (μ_B) when sites are filled. Qualitative values of μ_B of X and 1NN Ni atoms and total magnetism (calculations were conducted on $3 \times 3 \times 3$ super-cells) are reported in Table 4.

In the bulk, Ni atoms have a magnetic moment equal to about 0.62 μ_B (in excellent agreement with experimental findings). Insertion always leads to a decrease in μ_B of the first neighboring Ni atoms around the interstitial, especially when the system is filled by C and N atoms, whereas the magnetic moment of the interstitial atoms is always close to zero. Regarding the magnetic moment of the 2NN Ni atoms (not given here), the effect is low. For example, even when *M* sites are occupied by C or N atoms, the magnetism of 2NN Ni atoms remains unchanged. These results reinforce the conclusion that C and N atoms behave similarly in Ni.

In the case of oxygen, the magnetism on O atoms is low (negligible), compensating for the decrease in magnetism of Ni atoms close to O atoms. For H atoms, as seen above through the charge transfer and *eDOS* analyses, insertion only has a local effect on the lattice.

3.6. Effect of relaxation on site stability

Interactions between the add-atom and nickel are now discussed. The steric and elastic effects due to insertion were quantified by volume analysis, using (i) Ω_f, the volume of formation ($\Omega_f = V[N \cdot Ni + X] - V[N \cdot Ni]$, where V are the volumes of the system with and without impurity) which represents to overall effect of insertion on the lattice, (ii) δV_{voro} which corresponds to the difference in Voronoï volume [49] of the *i* site when filled or when free (local distortion), and (iii) $\Delta\mathscr{V}$, which is the difference between Ω_f and δV_{voro}. Data are summarized in Table 5.

The volumes of formation (Ω_f) are equal to 0.93, 2.24, 4.87 and 7.31 Å^3 for H, C, N and O atoms in *o* sites, respectively. As expected, Ω_f increases with the size of the interstitial atom. The same effect can also be observed for *t* and *M* sites. Ω_f is almost twice as large for *t* sites than for *o* sites, which illustrates a higher lattice distortion when *t* sites are filled as compared to *o* sites. In first-order approximation, it can be explained by the fact that *o* sites are larger than *t* sites, the insertion is thus easier. The analysis of steric effects shows that, from C to O, the distortion becomes more and more severe, that which is likely to reduce the stability of the system. We also found that when C or N atoms are in *M* sites, the volume of formation is smaller than in *t* sites. This shows that these species strongly interact with the first-nearest-neighboring nickel, to minimize their elastic energy.

The evolution of the volume of Voronoï, $\mathscr{V}$, which illustrates the local distortion, follows the same trend. To analyze it, we defined $\delta\mathscr{V}$, the difference in Voronoï volume when the site is filled and when it is free. The volumes of Voronoï of free *o*, *t* and *M* sites are respectively equal to 5.44, 5.76 and 5.72 Å^3. Special attention must be paid to the value of $\mathscr{V}$. Indeed, the largest volume of Voronoï does not correspond to *o* sites but to *t* sites: the volumes of Voronoï, which are computed taking into account distances between the nearest atoms, are conducted on anisotropic configurations. $\delta\mathscr{V}$ for *o* sites is thus found equal to 0.4, 0.9, 0.9 and 1.5 Å^3 for H, C, N and O atoms, respectively. The increase of $\delta\mathscr{V}$ with the size of the interstitial agrees with the fact that the local distortion increases with the size of the interstitial. The same comment can be made for *t* and *M* sites. Again, there is only a small difference between C and N atoms regarding volumes, this justifies that they have similar

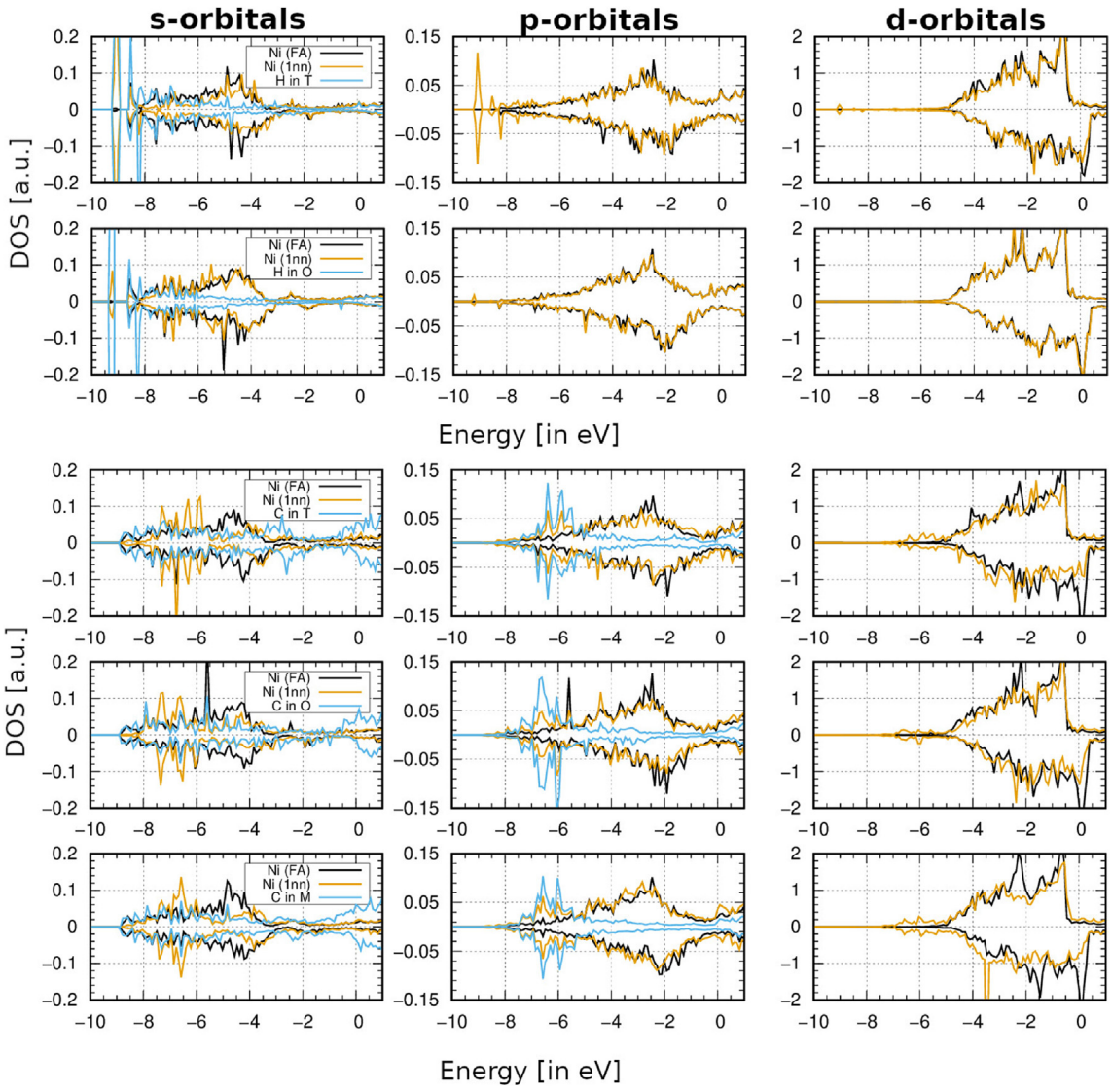

Fig. 4. Electronic density-of-states of H and C in *o*, *t* and *M* sites. The blue lines correspond to the *eDOS* of the interstitial species, the yellow lines of the 1NN Ni atoms of the X atom, and the black lines are the densities of the others Ni atoms. The DOS of the electrons are respectively projected on the *s* orbitals (plot on the left side), *p* orbitals (plot in the center) and *d* orbitals (plot on the right side). The positive (resp. negative) part of the *eDOS* corresponds to spin up (resp. down). (For interpretation of the references to colour in this figure legend, the reader is referred to the Web version of this article.)

behaviors in nickel.

The difference, $\Delta\mathscr{V}$, between the volume of formation Ω_f and of Voronoï $\delta\mathscr{V}$, see Table 6, which corresponds to the non-local deformation, or the deformation beyond the 1NN nickel atoms, is of 60, 60, 82 and 79% of Ω_f for H, C, N and O atoms in *o* sites, respectively. Since this increase can not be explained only by the increase in atomic size, electronic interactions are therefore responsible for this effect.

3.7. Elastic dipole

Finally, we discuss the effect of insertion in a continuous elasticity context. As explained by Clouet et al. [50] the insertion of an atom (or a point defect) into a lattice in a continuum description of elasticity can be modeled by a dipole tensor, $\mathscr{P}_{ij}$. This makes it possible to characterize elastic interactions between interstitial elements and other lattice defects (vacancies, grain-boundaries, etc.). To compute them, we followed the same approach as described in Ref. [51], but due to the excessive numerical cost (magnetism and many electrons in the pseudo-potential of nickel), the convergence tests of $\mathscr{P}_{ij}$ versus the super-cell size were limited to 216 atoms (see Fig. 6). Converged values are given in Table 6.

In the case of *t* and *o* sites, and by symmetry, the tensor is diagonal, and all components are equal ($\mathscr{P}_{11}$, for instance). As for the analysis of volumes, we note a significant increase in the components between *o* and *t* sites. These results can thus be correlated to the formation energies, *o* sites are always more stable than the others. From C to O atoms, $\mathscr{P}_{ij}$ increases with the electro-negativity of guest atoms. One notes that, in the case of the H atom, the elastic distortion on Ni lattice is very low. Not surprisingly, H atoms induce a very low and local distortion of the lattice, which is likely to have little effect on the elastic properties of fcc-Ni. The interaction is short ranged. By comparing hydrogen to other interstitials, we can see that the effect of H insertion is small. The elastic components of the other elements are of higher value, which implies strong long-range steric effects on the lattice. These results are consistent with the fact that C, N and O atoms have a low solubility limit compared to H atoms: this can be explained by evolution of Ω_f, as stated

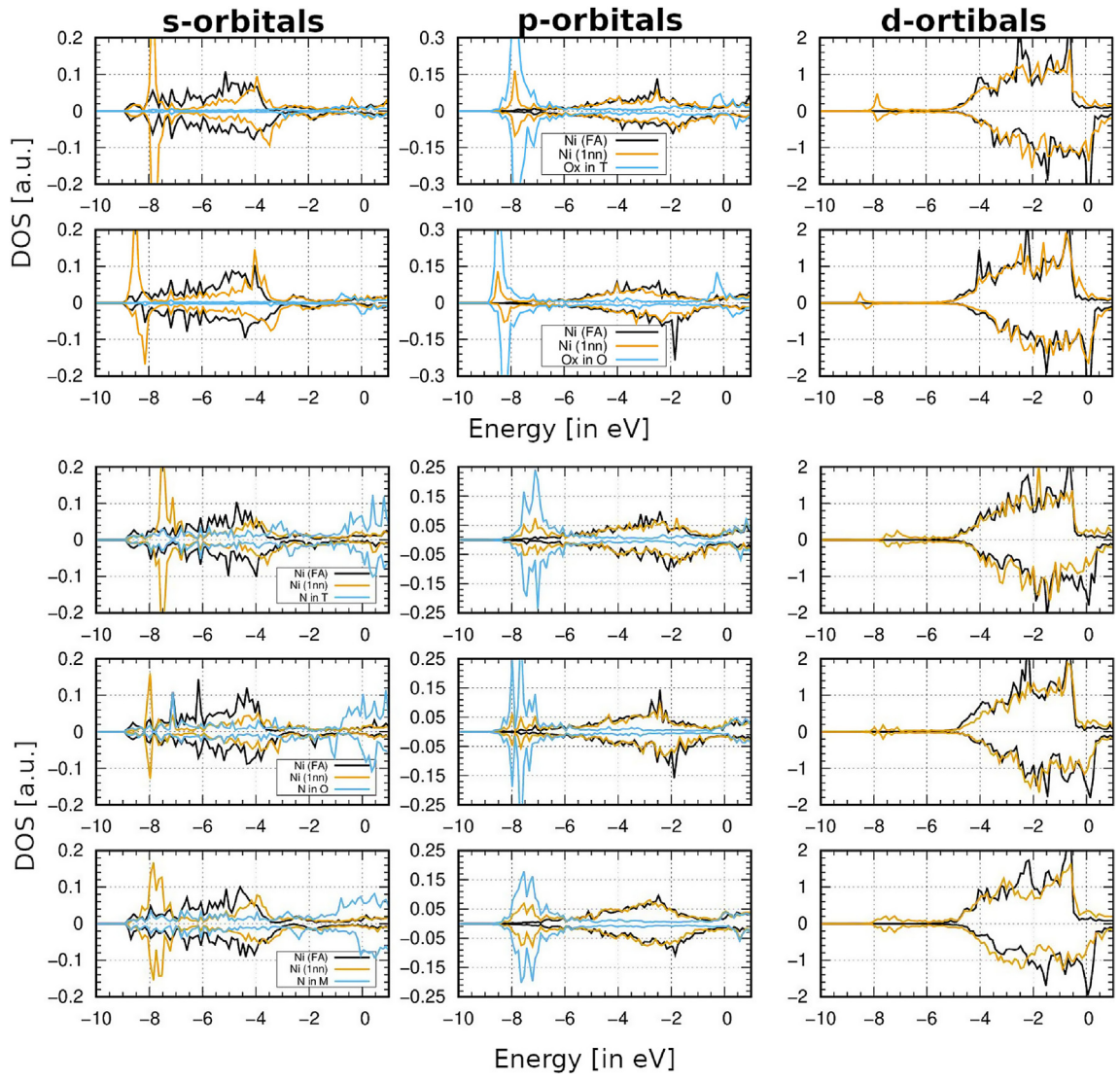

Fig. 5. *eDOS* of O and N atoms in *o*, *t* and *M* sites.

Table 4
Atomic magnetic moment (in μ_B) of the interstitial atom and the 1NN Ni atom of the interstitial. The total magnetic moments of the super-cells, μ_B^{tot}, were reported too. For information, the total magnetic moment of the free super-cell is equal to $68.15\mu_B$.

	config.	$\mu_B[X]$	$\mu_B^{1NN}[Ni]$	μ_B^{tot}
H	*o*	−0.05	0.47	67.44
	t	−0.07	0.54	67.36
C	*o*	−0.02	0.18	64.94
	t	−0.03	0.14	65.14
	M	−0.02	0.12	65.07
N	*o*	0.00	0.21	65.02
	t	−0.02	0.15	65.26
	M	0.00	0.14	65.56
O	*o*	0.15	0.57	67.96
	t	0.12	0.53	67.90

Table 5
Calculated valuers of the volume of formation (Ω_f in Å^3) and of Voronoï ($\mathscr{V}_{voro}$ in Å^3), and difference between the volume of formation and of Voronoï $\Delta\mathscr{V}$ (in Å^3). The free *o*, *t* and *M* volumes of Voronoï are equal to 5.44, 5.76 and 5.72 Å^3, respectively.

	conf.	Ω_f	$\delta\mathscr{V}_{voro}$	$\Delta\mathscr{V}$
H	*o*	0.93	0.37	0.56
	t	2.43	0.91	1.52
C	*o*	2.24	0.90	1.34
	t	6.34	2.21	4.13
	M	6.11	1.28	4.83
N	*o*	4.87	0.87	4.00
	t	7.55	2.15	5.40
	M	6.31	1.28	5.03
O	*o*	7.31	1.54	5.77
	t	14.08	2.70	11.38

above.

On the other hand, interstitials located in *M* sites induce strong anisotropic elastic strains (especially $\mathscr{P}_{11}$). The small value of $\mathscr{P}_{33}$ for *M* sites, as compared to *o* and *t* sites, can explain why, in the case of C atoms, this configuration is energetically more stable than *t* sites. It can be expected that, due to the important difference between in $\mathscr{P}_{11}$ values in *o* and *t* sites, diffusion mechanisms will induce high migration energies.

From these values, the effect of interstitial on lattice parameters can be evaluated using [51]:

Table 6
Calculated values of the elastic dipole tensor, $\mathscr{P}_{ij}$ (in eV), the relaxation volume tensor, $\mathscr{V}_{ij}$ (in Å^3), and the insertion energy at fixed lattice, E_i (in eV), and its relaxation volume, V_r (in Å^3), for 3 × 3 × 3 super-cells. In parentheses, we give the interaction energy (in meV). $\mathbb{I}$ is the matrix identity.

site	H	C	N	O
Elastic dipole tensor $\mathscr{P}_{ij}$,				
o	2.8 $\mathbb{I}$	9.2 $\mathbb{I}$	9.7 $\mathbb{I}$	12.9 $\mathbb{I}$
t	4.0 $\mathbb{I}$	12.6 $\mathbb{I}$	13.1 $\mathbb{I}$	15.2 $\mathbb{I}$
M	–	$\begin{bmatrix} 15.0 & 10.3 & 0 \\ 10.3 & 15.0 & 0 \\ 0 & 0 & 5.6 \end{bmatrix}$	$\begin{bmatrix} 16.4 & 9.8 & 0 \\ 9.8 & 16.4 & 0 \\ 0 & 0 & 5.2 \end{bmatrix}$	–
Relaxation volume tensor $\mathscr{V}_{ij}$,				
o	0.7 $\mathbb{I}$	2.6 $\mathbb{I}$	2.7 $\mathbb{I}$	3.6 $\mathbb{I}$
t	1.1 $\mathbb{I}$	3.5 $\mathbb{I}$	3.7 $\mathbb{I}$	4.2 $\mathbb{I}$
M	–	$\begin{bmatrix} 4.1 & 2.8 & 0 \\ 2.8 & 4.1 & 0 \\ 0 & 0 & 1.6 \end{bmatrix}$	$\begin{bmatrix} 4.4 & 2.6 & 0 \\ 2.6 & 4.4 & 0 \\ 0 & 0 & 1.6 \end{bmatrix}$	–

	E_i	V_r	E_i	V_r	E_i	V_r	E_i	V_r
o	0.071 (2)	2.2	0.609 (19)	7.7	0.732 (20)	8.0	0.514 (36)	10.7
t	0.334 (3)	3.3	2.304 (35)	10.6	1.806 (38)	10.9	0.712 (51)	12.7
M	–	–	2.296 (81)	9.9	2.360 (82)	10.5	–	–

$$a(C[X]) = a_o \cdot (1 + \delta \cdot C[X]) \tag{9}$$

where

$$\delta = \frac{4}{a_o^3}\frac{\mathscr{P}_{11}}{3B} = u \cdot \mathscr{P}_{11} \tag{10}$$

B is the bulk modulus, approximately equal to 198 GPa [47] and a_o the lattice parameter of the bulk, 3.52 Å. This gives $u = 0.075\ eV^{-1}$, $\mathscr{P}_{11}$ is thus expressed in eV.

By following the work of Varvenne et al. [52], the relaxation volumes (as well as the tensors $\mathscr{V}_{ij}$) and the interaction energies with periodic images were computed for 3 × 3 × 3 super-cells (which are generally used to study the insertion). We used the (theoretical) elastic constants of nickel, i.e. 274, 160 and 130 GPa [47] for C_{11}, C_{12} and C_{44}, respectively. Results are given in Table 6. Qualitatively and quantitatively, the relaxation volumes are in agreement with the volume of formation calculated on 3 × 3 × 3 super-cells. These results confirm the effect of relaxation can be captured by elastic theory. The results also show that the interaction energies due to periodic images are low, especially in the case of the H atom (< 3 meV). The elastic effects are greatest when C and N occupy *M* sites (about 80 meV). As shown by Varvenne et al. [52], DFT calculations at fixed volume therefore lead to accurate insertion energies taking into account correctly elasticity.

3.8. Effect of temperature

We conclude this part by discussing the effect of temperature on formation energies and configuration stability within the quasi-harmonic approximation. So as to take into account the effect of temperature, we considered that insertion does not affect the coefficient of thermal expansion of nickel (dilute limit). Eq. (1) was first used to set lattice parameters through lattice expansion of each configuration at different specific temperatures. It corresponds to a homogeneous dilatation of the shape of the super-cells (optimized at 0 K) including (or not) an interstitial specie: values are 1.0067, 1.0164, 1.0218 and 1.0276 a_o for the temperature of 600, 1200, 1500 and 1800 K, respectively. Energies and frequencies were then calculated using these parameters. Table 7 shows DFT energies (E^s) and vibrational Gibbs energies (which is equal to the Helmholtz free energy). Simulations were conducted at ambient pressure, p = 0 GPa. G^s_{vib} was calculated for different temperatures (0, 300, 600, 1200, 1500 and 1800 K):

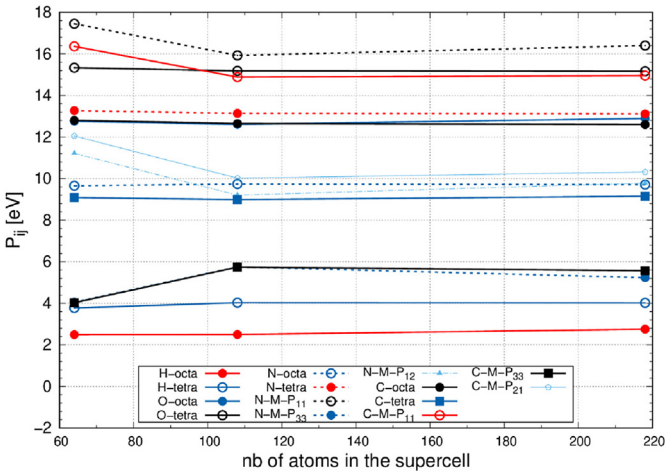

Fig. 6. Evolution of the elastic tensor $\mathscr{P}_{11}$ (in eV) as a function of super-cell size.

$$G^s_{vib}[X](T) = F_{vib}[n \cdot Ni + X](T) - F_{vib}[n \cdot Ni](T) - 0.5F_{ref}[X](T) - 0.5F^{ref}_{0K} \tag{11}$$

This equation includes (i) the effect of T on the free energy of reference states (gas or diamond), $F_{ref}[X](T)$ (see details summarized in Appendix A), and (ii) the difference in phonon free energies of the super-cell with and without an X atom, calculated at temperature T with the value of lattice parameter for the same T.

The Gibbs energy of insertion, G^s_{tot}, is thus the sum of E^s and G^s_{vib}.

Up to the melting point, there is no specific change in phonon properties. Octahedral sites are always the most stable sites and *M* sites still remain stable for C and N atoms. From a quantitative stand-point, we note that internal energy (E^s) slightly increases with T in most cases. Qualitatively, we note that the evolution of G^s_{tot} is mainly due to the vibrational component of the Gibbs energy. G^s_{tot} varies significantly with temperature due to the translational part of the partition function of the gas (p = 1 atm was chosen), see Appendix A.

It can also be noted that, between simulations performed at 0 and 1800K, the main change is associated with E^s (about 0.5 eV). The lattice expansion does not significantly change the value of G^s_{vib}, see Figure 7.

As explained, our approach was inspired by Wimmer's work. We can thus compare our results on H atoms with those of Wimmer [15]. He performed two calculations at two temperatures (0 and 1500 K). We only notice differences in energies for the calculations at 1500 K. When T increases, he sees that the formation energies decrease, unlike us. In his simulations "the lattice parameters of the super-cells (without and with H atoms) were kept at the computed value of a pure nickel crystal". Therefore, they did not include the specific relaxation of the cell when inserting H atoms in *o* or *t* sites, before to expand the lattice, contrary to our approach, as explained above. The energies of systems with interstitials are thus smaller in their cases than ours, especially in the case of *t* site (additional calculations were done with exactly the same approach to confirm it). The change in energy with lattice parameters is thus large, about 200 meV, in agreement with the difference observed.

Table 7
Internal energies (E^s, in eV) and vibrational enthalpies (G^s_{vib}, in eV) for different temperatures: 0, 600, 1200, 1500 and 1800 K.

atom	site	0 K		600 K		1200 K		1500 K		1800 K	
		E^s	G^s_{vib}	E^s	G^s_{vib}	E^s	G^s_{vib}	E^s	G^s_{vib}	E^s	G^s_{vib}
H	*o*	0.06	0.01	0.08	0.31	0.11	0.61	0.14	0.89	0.17	1.05
	t	0.32	0.08	0.35	0.41	0.39	0.70	0.43	0.97	0.46	1.16
C	*o*	0.59	0.09	0.59	−0.05	0.59	−0.31	0.61	−0.38	0.63	−0.52
	M	2.17	0.03	2.28	−0.30	2.44	−0.80	2.54	−1.06	2.62	−1.32
N	*o*	0.70	0.01	0.81	0.46	0.95	0.91	1.04	1.22	1.13	1.46
	t	1.76	0.00	1.88	0.35	2.02	0.67	2.12	0.86	2.20	1.02
	M	2.24	−0.03	2.25	0.23	2.27	0.52	2.30	0.55	2.32	0.67
O	*o*	0.47	−0.02	0.58	0.30	0.73	0.55	0.82	0.78	0.91	0.90
	t	0.65	0.00	0.75	0.30	0.88	0.55	0.97	0.75	1.05	0.87

4. Diffusion

4.1. Mechanisms

We will now discuss the diffusion of interstitials in dilute solution; traps (vacancies, precipitates, dislocations, etc.) were neglected in this approach. We took into consideration all possible stable positions and thus all possible paths.

As shown for Al [10], complex paths could exist in fcc systems, even in the case of interstitials, we must therefore take into account the full energy landscape of the network. The vibrations of the transition states (and the network) were also included in the study. Based on our preliminary results, some direct jumps were ruled out from the description of the diffusion. As shown previously, *M* is unstable with two imaginary frequencies for H and O atoms, whereas in the case of C and N atoms, *M* is an additional stable position. The existence of a stable *M* site thus modified the diffusion paths that should be considered.

To eliminate additional paths, tests were conducted with *M*-*M* direct jumps. They were unsuccessful: due to the small distance ($\sqrt{2}a_o/4$), equivalent to the *o*-*M* distance, NEB simulations indicate that, in all cases, the interstitial falls into an adjacent *o* site. Hence, there is no direct path between *M* sites. In the case of carbon, the NEB along the *o*-*t* path does not show a transition state, in agreement with literature data [8,53].

In conclusion, for H and O atoms, only one path is necessary to describe atomic diffusion (the one along *t*-*o*). In the case of nitrogen, there are three diffusion paths: *o*-*t*, *o*-*M* and *t*-*M* (see Fig. 8) and in the case of C atoms, only one jump has to be considered (along *o*-*M* path). As specified in section 2, CI-NEB calculations were

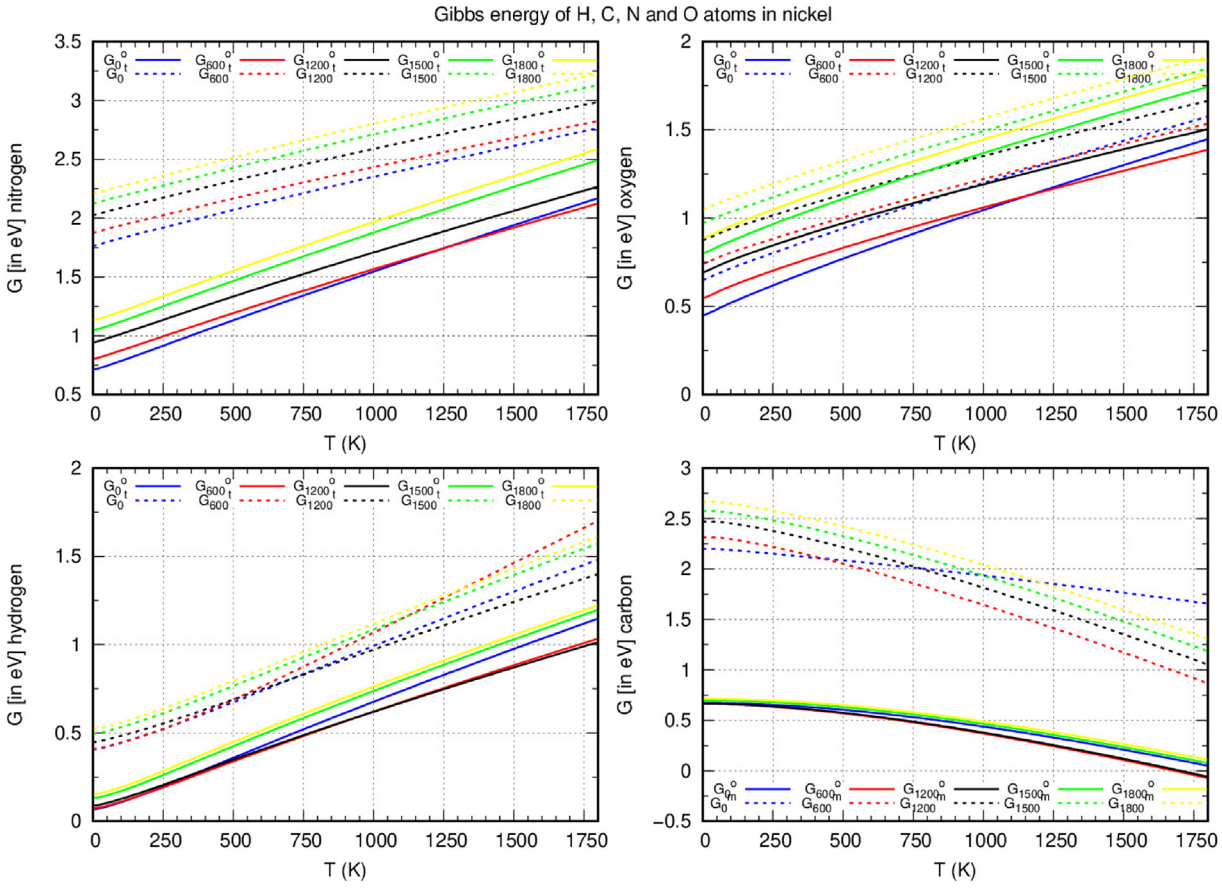

Fig. 7. Evolution of the Gibbs energies with temperature, for different values of lattice parameters corresponding to five temperatures, see text.

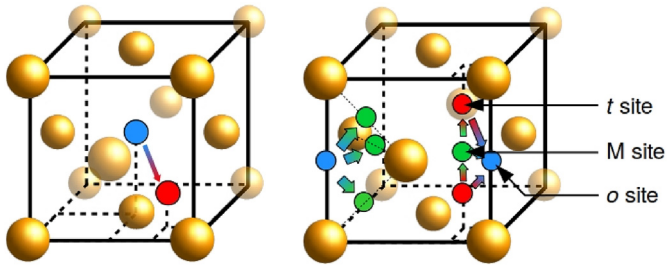

Fig. 8. Schematic representation of possible jumps when *t* and *o* sites are stable (a) and when there are *t*, *o* and *M* sites (b).

conducted to compute migration energies and the finite displacement method was used to compute inter-atomic forces. NEB simulations are plotted in Fig. 9.

From NEB calculations, migration energies and position of transition states were obtained. Inter-atomic forces of transition states were then calculated in order to compute frequency attempts, Γ_{xy} (see details in Appendix B). Migration energies are listed in Table 8.

The migration energies (E_m) of the diffusion along *o*-*t* for H and O atoms are equal to 0.41/0.15 and 0.75/0.53 eV, respectively. These values are relatively low. For hydrogen, the transition state is located in the triangle formed by the three Ni atoms that composed one of the faces of the tetrahedron, which is two-thirds of the distance between *o* and *t* sites. The small migration energy value of H atom can be explained by its small size and its weak electronic interaction with nickel atoms (localized charge density, Fig. 3). For oxygen, despite its strong interaction with the metal, E_m values are low. Its transition state is located at the midpoint of the *o* and *t* sites.

Concerning the migration of C and N atoms along the *o*-*M* path, barriers are similar, they are equal to the energy difference between *o* and *M* sites: the energy needed to leave the *M* site is low, less than 10 meV. For N atoms, E_m is about the same along *o*-*t* and *o*-*M* paths. Therefore, all paths should be taken into account in order to calculate diffusion coefficients. The position of the saddle points along the *o*-*o* path are smaller than the mean-square displacement of atoms, $\overline{d}_T$, presented above. Oscillations due to temperature lead to rule out *M* sites as they are unstable. We choose to neglect them hereinafter for simplification purposes. We will further compare our results against experimental data, basing our discussion on the

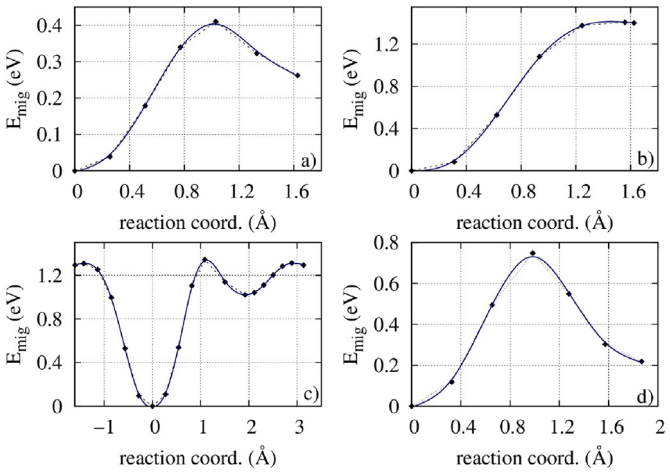

Fig. 9. NEB calculations for a) H along the path *o*-*t*, b) C along the path *o*-*M*, c) N along the path *M*-*o*-*t*-*M* and d) O along the path *o*-*t*. Continuous lines are interpolations drawn using a spline function of third degree applied by segment on the data points.

Table 8
Migration energies (in eV) for paths.

	H	C	N	O
$o \Rightarrow t$	0.41	–	1.34	0.75
$t \Rightarrow o$	0.15	–	0.32	0.53
$o \Rightarrow M$	–	1.42	1.31	–
$M \Rightarrow o$	–	0.02	0.02	–
$t \Rightarrow M$	–	–	0.29	–
$M \Rightarrow t$	–	–	0.02	–

calculation of the diffusion coefficient.

These results are consistent with theoretical literature. For H atoms, Wimmer [15] and Wang [12] found 0.47 and 0.44 eV, respectively; 0.53/0.70 eV [9] for oxygen; and 0.28/1.31 eV [9] for N atoms. The difference with Fang's results [14] are probably due to the functional they used (LDA), which reproduces with less precision properties of metallic systems. Regarding the *o*-*o* path for carbon, Siegel and Hamilton [8] and Connétable et al. [9] found a value equivalent to ours, i.e. 1.62 and 1.65 eV, respectively.

4.2. Effects of temperature

As was done for solubility, we evaluated the effect of temperature on migration energies. Two additional temperatures were considered: 600 and 1200 K. NEB simulations were then performed at fixed shapes, imposed by lattice thermal expansion on $2 \times 2 \times 2$ super-cells. Plots of the migration energies for paths of all species at 0, 600 and 1200 K are displayed in Fig. 10 to show the tendency.

Results show that the effect on migration energies of the dilatation induced by the temperature is low. From a numerical standpoint, migration energies slightly evolve, the maximum is about 20 meV. Moreover, the positions of transition states are unchanged with T. At this stage of approximation, this effect can be neglected, and we considered that values at 0 K are sufficient to capture the physics qualitatively and quantitatively.

4.3. Diffusion coefficients

We finally computed diffusion coefficients using DFT values reported previously. Explicit expressions of coefficients, taking into account only first-order transition states, are given in Appendix B.

To compute jump rates, Γ, frequencies were fully computed, using the initial states and the transition states. $D(T)$ were then computed and plotted, see Fig. 11. We also fit it with an Arrhenius

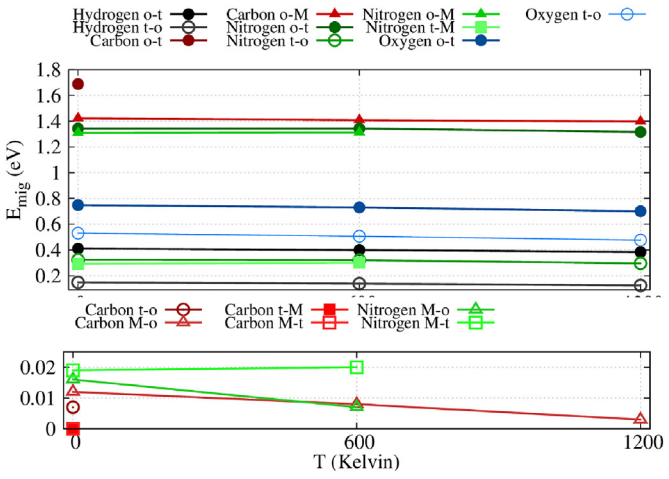

Fig. 10. Migration energy evolution as a function of T for interstitial atoms.

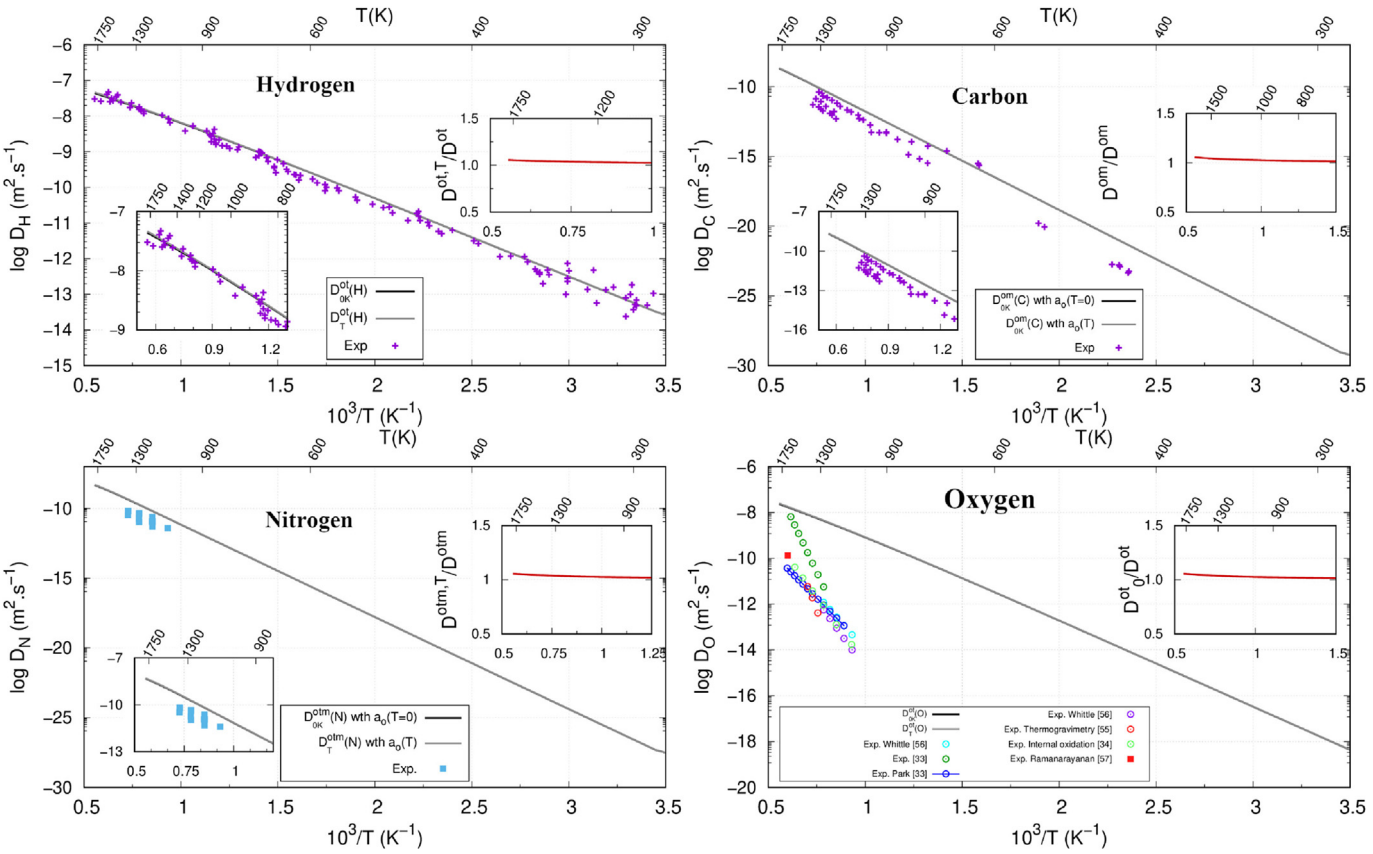

Fig. 11. Diffusion coefficients comparison against experimental data. Experimental values are extracted from the work of Berry for carbon [54], from the paper of Wimmer for hydrogen [15], from Krupp for nitrogen [55] and from Prillieux for oxygen [34,35,56–58]. We also plotted the coefficient diffusion supposing that the lattice parameter evolves with temperature, eq. (1).

law,

$$D(T) = D_o \exp(-E_a / k_B T), \tag{12}$$

to obtain D_o and activation energies (E_a). These parameters are summarized in Table 9.

We see that, apart from oxygen, theoretical and experimental values of D are in excellent agreement. Activation energies and D_o agree well with the literature (see Table 9). Theory is able to capture atomic scale diffusion mechanisms. The disagreement observed for O atoms is then attributed to the fact that oxygen interacts strongly with nickel and is not in interstitial form in nickel but in the form of clusters. Its diffusion mechanism is therefore highly dependent on the experimental conditions under which diffusivity measurements are performed (see discussion in Ref. [28]).

5. Conclusion

In this manuscript, we presented a complete study of the insertion and diffusion of interstitial species: carbon, nitrogen and oxygen. Results were compared to those of hydrogen. We first confirmed that all interstitial elements in nickel prefer to sit in octahedral sites. We also identified that, as in aluminum [10], C and N atoms admit one additional stable configuration that must be taken into consideration: the *M* site. However, the existence of *M* sites does not change the fact that *o* sites remain the most stable interstitial sites. We also showed that for C atoms, *t* sites are (elastically) unstable. Based on electronic properties, magnetic properties, charge transfers and elastic dipoles, we explained why *o* sites are more stable than the others.

We were able to quantify the local distortion effects (volumes of Voronoï) of those with long ranges (volumes of formation and

Table 9
Activation energies (E_a, in eV) and diffusion coefficient (D_o, in m^2/s) obtained from an Arrhenius fit: theoretical-experimental data comparison.

	H	C	N	O
E_a (in eV)				
This Work	0.42	1.40	1.28	0.94
Theo.	0.47 [15], 0.41 [9]	1.72 [8], 1.68 [9]	1.33 [9]	0.71 [9]
Exp.	0.42 [59]	1.54–1.71 [60–62]	1.30 [63]	
D_o (in m^2/s)				
This work	$9.5\ 10^{-7}$	$2.0\ 10^{-5}$	$2.1\ 10^{-5}$	$2.5\ 10^{-6}$
Theo.	$38.4\ 10^{-7}$ [15], $13.1\ 10^{-7}$ [9]	$0.63\ 10^{-5}$[9]	$0.18\ 10^{-5}$[9]	$1.15\ 10^{-6}$[9]
Exp.	$1.8–6.9\ 10^{-7}$ [59,64]	–	$4.6\ 10^{-5}$[63]	

elastic dipoles). Competition between elastic and electronic effects show a strong interaction between interstitials and nickel, especially for C and O atoms. We also showed that O and H atoms on one hand, and C and N atoms on the other hand have similar behaviors. The effects of temperature on migration energies was show to be is relatively limited, as compared to other processes that can take place in the material (cluster formation, interactions with traps, etc.).

When studying the diffusion of interstitial species, we meticulously took into account all different paths and analyzed each possibility. We gave here new explicit expressions of diffusion that takes into account the different configurations. Finally, we showed that DFT simulations and multi-state model reproduce experimental diffusion coefficients with accuracy, except for O atoms.

Declaration of competing interest

The authors declare that they have no known competing financial interests or personal relationships that could have appeared to influence the work reported in this paper.

CRediT authorship contribution statement

Matthieu David: Conceptualization, Methodology, Writing - original draft. **Aurélien Prillieux:** Conceptualization, Writing - review & editing. **Daniel Monceau:** Conceptualization, Writing - review & editing. **Damien Connétable:** Conceptualization, Data curation, Methodology, Project administration, Supervision.

Acknowledgments

This work was performed using HPC resources from CALMIP (Grant 2017-p0749, 2017-p0912 and 2018-p0912) and GENCI-CINES (Grant 2016-c2016097722 and A0020907722). Authors acknowledge M.-L. Doublet (Institute Charles-Gerhardt of Montpellier) for his remarks.

Appendix A. Statistical model and parameter of the Helmholtz energy of the gas

The Helmholtz energy of a X_2 gas (without the ZPE contribution) can be expressed by Ref. [65]:

$$F_{ref}[X](T,p) = -k_BT\left[\frac{3}{2}\ln\left(\frac{T}{A_t}\right)+\ln\left(\frac{k_BT}{p}\right)+1-\ln\left(1-e^{-\Theta_v/T}\right)+\ln\left(\frac{T}{\sigma\Theta_r}\right)+\ln(q_e)\right] \tag{A.1}$$

where $A_t = h^2/2\pi mk_B$, $\Theta_v = h\nu_{gas}/k_B$ and $\Theta_r = \hbar^2/2I_rk_B$. The first terms correspond to the translational components of the partition function of the molecule X_2, $\ln(1-e^{-\Theta_v/T})$ corresponds to the vibrational component, $\ln\left(\frac{T}{\sigma\Theta_r}\right)$ to the rotational one and the last to the electronic one. Parameters used in the present work are listed in Table A.10, where $m = 2M$ (M atomic mass), $I_r = Md^2/2$ the moment of inertia. q_e is the electronic partition function considered here as constant (see Helrich [65]). Values are computed for the current work. In all calculations, the gas pressure, p, is set to 1 atm.

Table A.10
Θ_v and Θ_r (in K) are the vibrational and rotational temperatures defined in the equipartition approach of the partition function. A_t is in K·m^2. We also give values of different quantities used in the formula: I_r, the moment of inertia (in kg.m^2), d, the inter-atomic distance (in Å), σ and q_e. ω is the frequency (in meV) of the molecule and F_{0K}^{ref} is the zero-point energy of the molecule (in meV).

	ω(meV)	$A_t(10^{-20}$ K.m$^2)$	Θ_v(K)	Θ_r(K)	$I_r(10^{-46}$ kg·m$^2)$	d(Å)	σ	q_e	F_{0K}^{ref}(meV)
H_2	540	151.2	6266/6331 [65]	85.5/87.57 [65]	0.047	0.75	2	1	135
N_2	300	10.9	3481/3393 [65]	2.81/2.87 [65]	1.432	1.11	2	4	75
O_2	194	9.5	2249/2274 [65]	2.00/2.08 [65]	2.009	1.23	2	5	49

Appendix B. Diffusion coefficients

We indicate here different expressions of the diffusion coefficient regardless of stable positions and possible paths. These expressions cover all configurations. For H and O atoms, we used eq. (B.1), for C atom, we used eq. (B.6) and for N atoms eq. (B.4).

In the case where there are two stable positions (t and o) and only one path (for H and O atoms), the diffusion coefficient is thus expressed by:

$$D = \frac{a_o^2}{2}\frac{\Gamma_{ot}\Gamma_{to}}{\Gamma_{to}+2\Gamma_{ot}} \tag{B.1}$$

Γ_{xy} is the jump rate from x to y computed by using the following equation [66]:

$$\Gamma_{xy} = \frac{k_BT}{h}\frac{\mathcal{Z}_{TS}}{\mathcal{Z}_{EI}}\exp\left[-\frac{\Delta E_m^{xy}}{k_BT}\right] \tag{B.2}$$

where ΔE_m corresponds to the transition migration energy. $\mathcal{Z}_{TS}$ is the (vibrational) partition function for the transition state and $\mathcal{Z}_{EI}$ is the same quantity for the initial position. $\mathcal{Z}$ is expressed by:

$$F = -k_BT\ln\mathcal{Z} = k_BT\sum_{\mathbf{q}\nu}\ln\left(2\sinh\left[\frac{\hbar\omega_{\mathbf{q}\nu}}{2k_BT}\right]\right) \tag{B.3}$$

where $\omega_{\mathbf{q}\nu}$ are the frequencies of the ν mode in **q** point. Eq. (B.2) is valid regardless of the configuration of the transition state.

With the M position, there are three paths, t-o, t-M and o-M, as described in Ref. [10], and the formula becomes:

$$\begin{aligned}D_{tom} = \frac{a_o^2}{4}\Big[&6\,\Gamma_{mo}\Gamma_{om}\Gamma_{tm}+3\,\Gamma_{mt}\Gamma_{om}\Gamma_{tm}+6\,\Gamma_{mo}\Gamma_{ot}\Gamma_{tm}\\&+2\,\Gamma_{mt}\Gamma_{ot}\Gamma_{tm}+4\,\Gamma_{mo}\Gamma_{om}\Gamma_{to}+6\,\Gamma_{mt}\Gamma_{om}\Gamma_{to}+\\&4\,\Gamma_{mo}\Gamma_{ot}\Gamma_{to}+4\,\Gamma_{mt}\Gamma_{ot}\Gamma_{to}]/[6\,\Gamma_{mt}\Gamma_{om}\\&+4\,\Gamma_{mo}\Gamma_{ot}+4\,\Gamma_{mt}\Gamma_{ot}+3\,\Gamma_{mo}\Gamma_{tm}+18\,\Gamma_{om}\Gamma_{tm}\\&+12\,\Gamma_{ot}\Gamma_{tm}+2\,\Gamma_{mo}\Gamma_{to}+2\,\Gamma_{mt}\Gamma_{to}+12\,\Gamma_{om}\Gamma_{to}]\end{aligned} \tag{B.4}$$

If we now consider three stable sites (t, o and M) but only t-M and o-M jumps, D is thus expressed as:

$$D = \frac{a_o^2}{4} \frac{(2\,\Gamma_{mo} + \Gamma_{mt})\Gamma_{om}\Gamma_{tm}}{(2\,\Gamma_{mt}\Gamma_{om} + \Gamma_{mo}\Gamma_{tm} + 6\,\Gamma_{om}\Gamma_{tm})} \quad \text{(B.5)}$$

Finally, the diffusion coefficient becomes:

$$D = \frac{a_o^2}{2} \frac{\Gamma_{mo}\Gamma_{om}}{\Gamma_{mo} + 6\,\Gamma_{om}} \quad \text{(B.6)}$$

if we do not consider *t* sites as stable, but only *o* and *M* sites. Formula were derived as described in Ref. [10].

References

[1] H. Birnbaum, I. Robertson, P. Sofronis, D. Teter, Mechanisms of hydrogen related fracture-a review, in: Proceedings of CDI'96, Magnin ed., The Institute of Materials, 1997. Th.

[2] D.J. Young, J. Zhang, C. Geers, M. Schütze, Recent advances in understanding metal dusting: a review, Mater. Corros. 62 (1) (2011) 7–28, https://doi.org/10.1002/maco.201005675, arXiv, https://onlinelibrary.wiley.com/doi/pdf/10.1002/maco.201005675.

[3] D. Connétable, First-principles study of transition metal carbides, Mater. Res. Express 3 (12) (2016) 126502. 10.1088/2053-1591/3/12/126502.

[4] R. Molins, G. Hochstetter, J. Chassaigne, E. Andrieu, Oxidation effects on the fatigue crack growth behaviour of alloy 718 at high temperature, Acta Mater. 45 (2) (1997) 663–674, https://doi.org/10.1016/S1359-6454(96)00192-9.

[5] D. Young, High Temperature Oxidation and Corrosion of Metals, Elsevier Corrosion series, 2008.

[6] L. Iorio, M. Cortie, R. Jones, Technical Note: solubility of nitrogen in experimental low-nickel austenitic stainless steels, J. S. Afr. Inst. Min. Metall (1994) 173.

[7] B. Nabavi, M. Goodarzi, V. Amani, Nitrogen effect on the microstructure and mechanical properties of nickel alloys, Weld. J. 94 (February) (2015) 53.

[8] D. Siegel, J. Hamilton, First principles study of solubility diffusion and clustering ofc in ni, Phys. Rev. B 68 (2003), 094105.

[9] D. Connétable, E. Andrieu, D. Monceau, First-principles nickel database: energetics of impurities and defects, Comput. Mater. Sci. 101 (2015) 77–87.

[10] M. David, D. Connétable, Diffusion of interstitials in metallic systems, illustration of a complex study case: aluminum, J. Phys. Condens. Matter 29 (45) (2017) 455703. http://stacks.iop.org/0953-8984/29/i=45/a=455703.

[11] H.H. Wu, D.R. Trinkle, Direct diffusion through interpenetrating networks: oxygen in titanium, Phys. Rev. Lett. 107 (2011), 045504. 10.1103/PhysRevLett.107.045504.

[12] Y. Wang, D. Connétable, D. Tanguy, Hydrogen influence on diffusion in nickel from first-principles calculations, Phys. Rev. B 91 (2015), 094106.

[13] Y. Wang, D. Connétable, D. Tanguy, Influence of trap connectivity on h diffusion: vacancy trapping, Acta Mater. 103 (2016) 334–340.

[14] H. Fang, S. Shang, Y. Wang, Z. Liu, D. Alfonso, D. Alman, Y. Shin, C. Zou, A. van Duin, Y. Lei, G. Wang, First-principles studies on vacancy-modified interstitial diffusion mechanism of oxygen in nickel, associated with large-scale atomic simulation techniques, J. Appl. Phys. 115 (2014), 043501.

[15] E. Wimmer, W. Wolf, J. Sticht, P. Saxe, C.B. Geller, R. Najafabadi, G.A. Young, Temperature-dependent diffusion coefficients from ab initio computations: hydrogen, deuterium, and tritium in nickel, Phys. Rev. B 77 (2008) 134305. 10.1103/PhysRevB.77.134305.

[16] G. Kresse, J. Hafner, Ab initio molecular dynamics for liquid metals, Phys. Rev. B 47 (1993) 558R.

[17] J.P. Perdew, K. Burke, M. Ernzerhof, Generalized gradient approximation made simple, Phys. Rev. Lett. 77 (1996) 3865–3868. 10.1103/PhysRevLett.77.3865.

[18] P.E. Blöchl, Projector augmented-wave method, Phys. Rev. B 50 (1994) 17953–17979. 10.1103/PhysRevB.50.17953.

[19] G. Kresse, D. Joubert, From ultrasoft pseudopotentials to the projector augmented-wave method, Phys. Rev. B 59 (1999) 1758–1775. 10.1103/PhysRevB.59.1758.

[20] M. Černý, J. Pokluda, M. Šob, M. Friák, P. Šandera, Ab initio calculations of elastic and magnetic properties of fe, co, ni, and cr crystals under isotropic deformation, Phys. Rev. B 67 (2003), 035116. 10.1103/PhysRevB.67.035116.

[21] H.J. Monkhorst, J.D. Pack, Special points for brillouin-zone integrations, Phys. Rev. B 13 (1976) 5188–5192. 10.1103/PhysRevB.13.5188.

[22] A. Togo, F. Oba, I. Tanaka, First-principles calculations of the ferroelastic transition between rutile-type and $cacl_2$-type sio_2 at high pressures, Phys. Rev. B 78 (2008) 134106. 10.1103/PhysRevB.78.134106.

[23] G. Henkelman, Improved Tangent Estimate in the Nudged Elastic Band Method for Finding Minimum Energy Paths and Saddle Points 9978, 2000, https://doi.org/10.1063/1.1323224.

[24] D. Sheppard, P. Xiao, W. Chemelewski, D.D. Johnson, G. Henkelman, I. Introduction, A Generalized Solid-State Nudged Elastic Band Method 074103, 2012, pp. 1–8.

[25] A. Metsue, A. Oudriss, X. Feaugas, Hydrogen solubility and vacancy concentration in nickel single crystals at thermal equilibrium: new insights from statistical mechanics and ab initio calculations, J. Alloy. Comp. 656 (2016) 555–567, https://doi.org/10.1016/j.jallcom.2015.09.252.

[26] A.V. Subashiev, H.H. Nee, Hydrogen trapping at divacancies and impurity-vacancy complexes in nickel: first principles study, J. Nucl. Mater. 487 (2017) 135–142. 10.1016/j.jnucmat.2017.01.037.

[27] D. Connétable, M. David, A. Prillieux, D. Young, D. Monceau, Impact of the clusterization on the solubility of oxygen and vacancy concentration in nickel: a multi-scale approach, J. Alloy. Comp. 708 (2017) 1063–1072, https://doi.org/10.1016/j.jallcom.2017.03.018.

[28] D. Connétable, M. David, Diffusion of interstitial species (h and o atoms) in fcc systems (al, cu, co, ni and pd): contribution of first and second order transition states, J. Alloy. Comp. 772 (2019) 280–287, https://doi.org/10.1016/j.jallcom.2018.09.042.

[29] R. Nazarov, T. Hickel, J. Neugebauer, *Ab initio* study of h-vacancy interactions in fcc metals: implications for the formation of superabundant vacancies, Phys. Rev. B 89 (2014) 144108. 10.1103/PhysRevB.89.144108.

[30] A. Sieverts, The absorption of gases by metals, Z. Met. 21 (1929) 37–46.

[31] Y. Fukai, The Metal-Hydrogen System: Basic Bulk Properties, vol. 21, Springer Science & Business Media, 2006.

[32] D. Tanguy, Y. Wang, D. Connétable, Stability of vacancy-hydrogen clusters in nickel from first principles calculations, Acta Mater. 78 (2014) 135–143.

[33] A. Seybolt, Dissertation, Yale university, New Haven, CT, 1936.

[34] J.-W. Park, C. Altstetter, The diffusion and solubility of oxygen in solid nickel, Metall. Trans. A 18A (1987) 43.

[35] A. Prillieux, Hydrogen and water vapour effects on oxygen solubility and diffusivity in high temperature fe-ni alloys. http://oatao.univ-toulouse.fr/18676/.

[36] C. Wang, D. Solodovnikov, K. Lynn, Defauts ce@ y3al5o12, Phys. Rev. B 73 (2006) 233204.

[37] W.W. Dunn, R.B. Mclellan, W. Oates, The solubility of carbon in cobalt and nickel, Trans. AIME 242 (11) (1968).

[38] R. Abdulrahman, A. Hendry, The solubility of nitrogen in liquid pure nickel, Metall. Mater. Trans. B Process Metall. Mater. Process. Sci. 32 (6) (2001) 1095–1101. 10.1007/s11663-001-0097-4.

[39] V. Fedorchenko, V. Averin, A. Samarin, Solubility of nitrogen in liquid nickel and in nickel–chromium, nickel– molybdenum, and nickel–tungsten melts, Dokl. Akad. Nauk SSSR 183 (1968) 894–896. Dec. 1, 1968.

[40] Y. Kojima, M. Inouye, Y. Yamada, Solubility and diffusivity of nitrogen in liquid iron-nickel and iron-cobalt alloys at 1600°C, Trans. Iron Steel Inst. Jpn. 15 (12) (1975) 599–605.

[41] H. Wada, R.D. Pehlke, Solubility of nitrogen in liquid fe-cr-ni alloys containing manganese and molybdenum, Metall. Trans. B 8 (3) (1977) 675–682. 10.1007/BF02658639.

[42] D. Connétable, First-principles calculations of carbon clathrates: comparison to silicon and germanium clathrates, Phys. Rev. B 82 (2010), https://doi.org/10.1103/PhysRevB.82.075209, 075209.

[43] F. Mouhat, F.m. c.-X. Coudert, Necessary and sufficient elastic stability conditions in various crystal systems, Phys. Rev. B 90 (2014) 224104, https://doi.org/10.1103/PhysRevB.90.224104.

[44] A.B. Mei, O. Hellman, N. Wireklint, C.M. Schlepütz, D.G. Sangiovanni, B. Alling, A. Rockett, L. Hultman, I. Petrov, J.E. Greene, Dynamic and structural stability of cubic vanadium nitride, Phys. Rev. B 91 (2015), 054101. 10.1103/PhysRevB.91.054101.

[45] D.C. Wallace, Thermodynamics of Crystals, Courier Corporation, 1998.

[46] C. Kittel, Introduction to Solid State Physics, Wiley, New York, 1996.

[47] D. Connétable, O. Thomas, First-principles study of the structural, electronic, vibrational, and elastic properties of orthorhombic nisi, Phys. Rev. B 79 (2009), 094101. 10.1103/PhysRevB.79.094101.

[48] G. Henkelman, A. Arnaldsson, H. Jónsson, A fast and robust algorithm for bader decomposition of charge density, Comput. Mater. Sci. 36 (3) (2006) 354–360, https://doi.org/10.1016/j.commatsci.2005.04.010.

[49] C.H. Rycroft, Voro++: a three-dimensional voronoi cell library in c++, Chaos 19 (2009).

[50] E. Clouet, S. Garruchet, H. Nguyen, M. Perez, C.S. Becquart, Dislocation interaction with c in alpha-fe: a comparison between atomic simulations and elasticity theory, Acta Mater. 56 (14) (2008) 3450–3460. 10.1016/j.actamat.2008.03.024.

[51] D. Connétable, M. David, Study of vacancy-(h,b,c,n,o) clusters in al using dft and statistical approaches: consequences on solubility of solutes, J. Alloy. Comp. 748 (2018) 12–25, https://doi.org/10.1016/j.jallcom.2018.03.081.

[52] C. Varvenne, F. Bruneval, M.-C. Marinica, E. Clouet, Point defect modeling in materials: coupling ab initio and elasticity approaches, Phys. Rev. B 88 (2013) 134102. 10.1103/PhysRevB.88.134102.

[53] D. Connétable, E. Andrieu, D. Monceau, First-principles nickel database: energetics of impurities and defects, Comput. Mater. Sci. 101 (2015) 77–87.

[54] B.S. Berry, Diffusion of carbon in nickel, J. Appl. Phys. 44 (8) (1973) 3792–3793. 10.1063/1.1662846.

[55] U. Krupp, H.-J. Christ, Internal nitridation of nickel-base alloys. part i. behavior of binary and ternary alloys of the ni-cr-al-ti system, Oxid. Metals 52 (1998) 277.

[56] C.B. Alcock, P.B. Brown, Physicochemical factors in the dissolution of thoria in solid nickel, Met. Sci. J. 3 (1969) 116.

[57] T. Ramanarayanan, R. Rapp, Metall. Trans. 3 (1972) 3239.

[58] D. Whittle, Y. Shida, G. Wood, F. Stott, B. Bastow, Enhanced diffusion of oxygen during internal oxidation of nickel-base alloys, Philos. Mag. A 46 (6) (1982) 931–949.

[59] Y. Fukai, The Metal-Hydrogen System: Basic Bulk Properties, second ed., Springer-Verlag Berlin and Heidelberg GmbH & Co. K, 2003.
[60] J. Lander, H. Kern, A. Beach, Solubility and diffusion coefficient of carbon in nickel reaction rates of nickel-carbon alloys with barium oxide, J. Appl. Phys. 23 (1952) 1305.
[61] R. Smith, Trans. Metall. Soc. AIME 236 (1966) 1224.
[62] J. Cermak, H. Mehrer, Acta Metall. Mater. 42 (1994) 1345.
[63] U. Krupp, H.-J. Christ, Internal nitridation of nickel-base alloys. part ii. behavior of quaternary ni-cr-al-ti alloys and computer-based description, Oxid. Metals 52 (199) 314.
[64] J. Völkl, G. Alefeld, Hydrogen in Metlas, Springer, New York, 1978.
[65] C. Helrich, Modern Thermodynamics with Statistical Mechanics, Springer Berlin Heidelberg, 2008.
[66] H. Eyring, The activated complex in chemical reactions, J. Chem. Phys. 3 (2) (1935) 107−115, arXiv, 10.1063/1.1749604.